Moiré surface states and enhanced superconductivity in topological insulators

Taige Wang,[1,2,3] Noah F. Q. Yuan,[1,*] and Liang Fu[1]

[1] *Department of Physics, Massachusetts Institute of Technology, Cambridge, MA 02139, USA*

[2] *Department of Physics, University of California, San Diego, CA 92093, USA*

[3] *Department of Physics, University of California, Berkeley, CA 94720, USA*

(Dated: October 11, 2021)

Recently, moiré superlattices have been found on the surface of topological insulators (TI) due to the rotational misalignment of topmost layers. In this work, we study the effects of moiré superlattices on the topological surface states using a continuum model of Dirac electrons moving in a periodic potential. Unlike twisted bilayer graphene, moiré surface states cannot host isolated bands due to their topological nature. Instead, we find (high-order) van Hove singularities (VHS) in the moiré band structure that give rise to divergent density of states (DOS) and enhance interaction effects. Due to spin-momentum locking in moiré surface states, possible interaction channels are limited. In the presence of phonon mediated attraction, superconductivity is strongly enhanced by the power-law divergent DOS at high-order VHS. The transition temperature T_c exhibits a *power-law* dependence on the retarded electron-phonon interaction strength λ^*. This enhancement is found to be robust under various perturbations from the high-order VHS.

arXiv:2010.09753v3 [cond-mat.supr-con] 6 Feb 2021

I. INTRODUCTION

In recent years, moiré superlattices have been studied extensively in various 2D van der Waals heterostructures exemplified by graphene and transition metal dichalcogenide (TMD) multilayers [1–3]. These moiré systems exhibit a variety of remarkable electronic properties due to strong correlation effects in flat minibands. Besides graphene and TMD, another large family of moiré superlattices can be found in topological insulators [4–14]. When Bi_2Se_3 and Bi_2Te_3 bulk crystals are grown by the molecular-beam epitaxy (MBE), it is common to find a small rotational misalignment of topmost quintuple layers, leading to a moiré superlattice on the surface [5, 6]. Interestingly, a scanning tunneling microscope (STM) measurement [6] has directly observed such moiré superlattice in Bi_2Te_3 and found multiple sharp peaks in the local density of states (LDOS). Moreover, moiré superlattices can also be found in the van der Waals heterostructure of topological insulators and large-gap insulators [7–9, 13]. Despite the ubiquity of moiré superlattices in TI, their effects on topological surface states have not been studied theoretically.

In this letter, we study moiré surface states of TI. The topological nature of TI surface states prevents them from gap opening as long as time-reversal symmetry is preserved, hence the moiré surface states do not form isolated mini bands, unlike other moiré systems such as graphene and TMD. Instead, we find prominent van Hove singularities (VHS) in moiré surface states which give rise to divergent density of states (DOS). Under appropriate conditions, some of these VHS exhibit power-law divergent DOS, which are known as *high-order* VHS [15].

We further study interaction effects near (high-order) VHS enhanced by the divergent DOS [16–19]. In moiré surface states, possible interaction channels at VHS are limited due to spin-momentum locking. Under attractive interactions, superconductivity is favored. We find a new analytic formula for the electron-phonon superconducting critical temperature T_c (see Eq. (10)), which exhibits a *power-law* dependence of the retarded electron-phonon interaction λ^* and is thus parametrically enhanced with respect to the exponentially small T_c in ordinary metals and at ordinary VHS [20, 21]. Importantly, the absence of moire band gaps and the large electron velocity away from VHS facilitate the reduction of Coulomb repulsion through retardation effects. We also show that the enhancement of superconductivity is robust and persist even when the system is perturbed away from high-order VHS.

This work is organized as follows: we first introduce and study a model of moiré surface states as Dirac fermion in a periodic scalar potential in Sec. II. Within the model, we identify high-order VHS at the crosses of circular Fermi surfaces. Then, we solve the gap equation for the superconducting critical temperature T_c in the presence of power-law divergent density of states, taking account of both electron-phonon interaction and Coulomb repulsion within the Anderson-Morel approximation [22] (Sec. III). In the end, we discuss several experimental platforms to search for moiré surface states and enhanced superconductivity.

* Current address: Shenzhen JL Computational Science and Applied Research Institute, Shenzhen, 518109 China.

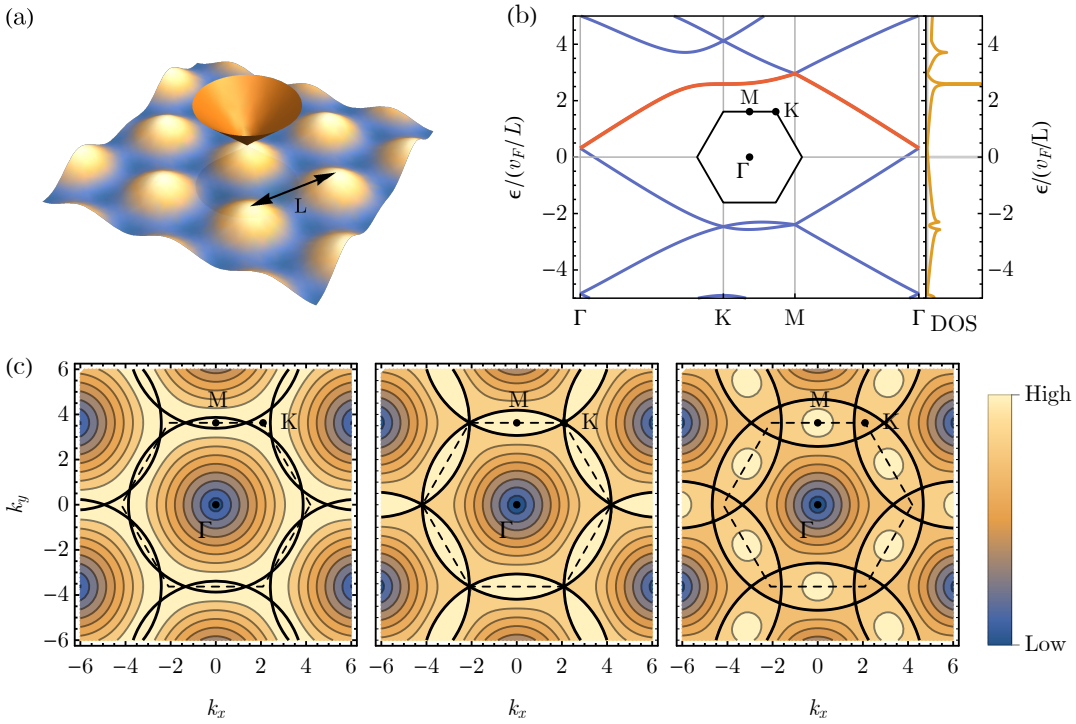


FIG. 1. (a) Dirac fermion in a C_3 periodic potential with superlattice constant L. (b) Left panel: spectrum at potential $U_c = 1.36v_F/L$. The corresponding mini BZ is shown in the center. The entire spectrum remains gapless due to the symmetry anomaly. Between the main Dirac point Γ and satellite Dirac points M (highlighted in red), we find a high-order van Hove singularity (VHS) at the K point. Right panel: corresponding density of state (DOS). The high-order VHS peak stands out, with several ordinary VHS accompanied. (c) Fermi surface at potential $U = 1.0v_F/L$, $1.36v_F/L$ and $1.7v_F/L$ from left to right. The ones passing through VHS are all perfect circles, which are plotted in thick black curves. When $U = 1.36v_F/L$, all three Fermi surfaces cross at the K point, making it a high-order VHS.

II. DIRAC FERMION IN A PERIODIC SCALAR POTENTIAL

In this section, we introduce and study a model of moiré topological insulator surface states as Dirac fermion in a periodic scalar potential. A previous DFT study in Bi_2Se_3/MoS_2 [7] revealed folded Dirac cones within the bulk gap due to the moiré superlattice. Thus, we start with the massless Dirac fermion in two dimensions (2D)

$$H_0(\boldsymbol{k}) = v_F(k_x\sigma^y - k_y\sigma^x), \tag{1}$$

where v_F is the Fermi velocity, $\boldsymbol{k} = (k_x, k_y)$ is the two-dimensional momentum, $\boldsymbol{\sigma} = (\sigma^x, \sigma^y)$ are the Pauli matrices. Now we allow the continuous translation symmetry be broken into discrete ones by the moiré superlattice, while leave the time-reversal symmetry intact. Then the lowest order perturbation can be described by a spin-independent periodic scalar potential $U(\boldsymbol{r})$:

$$H(\boldsymbol{k}, \boldsymbol{r}) = H_0(\boldsymbol{k}) + U(\boldsymbol{r})\sigma^0, \tag{2}$$

where σ^0 is the identity matrix, $U(\boldsymbol{r}) = U(\boldsymbol{r} + \boldsymbol{L}_{1,2})$, and the $\boldsymbol{L}_{1,2}$ are two primitive vectors of the moiré superlattice. A schematic diagram of this setup is shown in Fig. 1a. This model can apply to bulk TI crystals with top layers twisted or the surface state in the interface between a topological insulator (TI) and a large-gap insulator.

The density of states (DOS) of the system described by Eq. (2) generally looks like the right panel in Fig. 1b, where positive and negative sides are qualitatively similar. Near zero energy, DOS grows linearly. As energy increases, VHS peaks emerge. At higher energy, new Dirac points are formed (known as satellite Dirac points [23]), so that the entire spectrum remains gapless. Among these VHS peaks, there are a few prominent ones that are, in fact, high-order VHS peaks, given appropriate parameters.

In comparison to ordinary VHS that are caused by saddle points in the energy dispersion, such high-order VHS peaks are caused by high-order critical points $\boldsymbol{k}_c$ in momentum space, where the electron velocity and the Hessian matrix determinant both vanish, $\nabla E(\boldsymbol{k}_c) = \boldsymbol{0}$, $\det D(\boldsymbol{k}_c) = 0$, $(D_{ij} = \partial_i\partial_j E)$. Around these high-order VHS, the energy dispersion is characterized by high-order polynomials of momenta, and the DOS shows

power-law divergence [24],

$$N(\xi) = \begin{cases} C_+ \xi^\nu, & \xi > 0 \\ C_-(-\xi)^\nu, & \xi < 0 \end{cases}. \tag{3}$$

Here $-1 < \nu < 0$ is the power-law exponent and $C_\pm > 0$ are coefficients of the electron (hole) side. $E(\boldsymbol{k})$ denotes the energy dispersion and $\xi = E - E(\boldsymbol{k}_c)$.

To be concrete, we first consider a periodic potential as follows

$$U(\boldsymbol{r}) = 2U \sum_{j=1}^{3} \cos(\mathbf{G}_j \cdot \mathbf{r}), \tag{4}$$

where $\boldsymbol{G}_j = \frac{4\pi}{\sqrt{3}} L^{-1}(-\sin\frac{2\pi j}{3}, \cos\frac{2\pi j}{3})$ are three reciprocal vectors, and U is the potential strength. Then there are two energy scales v_F/L and U in Eq. (2), and the low-energy physics is determined by a single dimensionless control parameter UL/v_F.

As shown in the band structure (Fig. 1b), the first set of satellite Dirac points on positive side are found at M points, and there are generically six saddle points per moiré Brillouin zone (MBZ) between the main Dirac point Γ and satellite Dirac points M. Remarkably, the Fermi surfaces passing through these saddle points are all perfect circles in a wide range of UL/v_F (Fig. 1c).

When $U = 1.36 v_F/L$, three ordinary saddle points and one local extremum merge into a high-order saddle point at the K point where all three Fermi surfaces intersect (Fig. 1c), and the dispersion around the K point becomes flattened (Fig. 1b). In the experiment, the potential strength U and the Fermi velocity v_F are mostly determined by the material, but we can tune this parameter UL/v_F by tuning the twisted angle θ and the resulting superlattice constant $L = a/\theta$. Thus, we can also define a magic angle $\theta_c = 0.74Ua/v_F$ when our system hits high-order VHS, where a is the atomic lattice constant.

Among high symmetry points Γ, M and K, the time-reversal invariant points Γ, M will always be at least doubly degenerate, while only K point can become spin singlet. We can thus expand the singlet dispersion $E_{\boldsymbol{k}}$ around the K point,

$$E_{\boldsymbol{p}+\boldsymbol{K}} - E_{\boldsymbol{K}} = \alpha p^2 + \beta(p_x^3 - 3p_x p_y^2) + \gamma p^4 + \cdots \tag{5}$$

where $p^2 = p_x^2 + p_y^2$ with p_x (p_y) parallel (perpendicular) to the ΓK line. We then compute the Taylor coefficients α, β and γ as functions of UL/v_F as shown in Fig. 2a. When $U = 1.36 v_F/L$, we find α vanishes, while β remains finite, indicating a high-order saddle point described by a third-order polynomial $E_{\boldsymbol{p}+\boldsymbol{K}} - E_{\boldsymbol{K}} = \beta(p_x^3 - 3p_x p_y^2)$.

The density of states (DOS) of a C_3 saddle point diverges with power-law exponent $\nu = -1/3$ according to the scaling property of the dispersion [15, 24]. As shown in Fig. 2b, the numerical power-law fitting of DOS gives $\nu = -0.39$, which agrees well with $\nu = -1/3$.

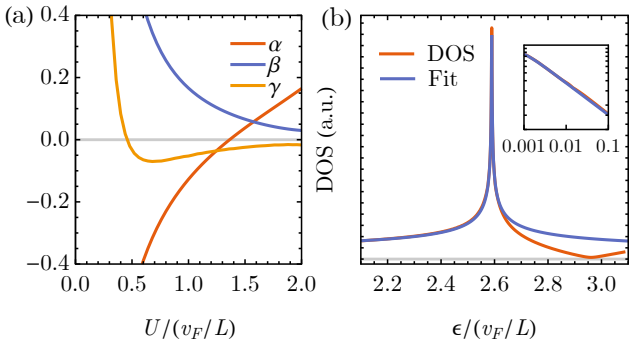


FIG. 2. (a) Dimensionless derivatives $\partial^n E/\partial p_x^n (v_F L^{n-1} n!)^{-1}$ of the moiré surface state dispersion with respect to momentum at the K point, where α, β, and γ correspond to $n = 2, 3$, and 4 (see Eq. (5) of main text). The potential is given in Eq. (4). When $UL/v_F = 1.36$, α vanishes, making the K point a high-order saddle point. (b) DOS around the high-order VHS. The log-log plot in the inset shows that the divergence of the DOS is indeed power-law. The fitting is given by $N(\epsilon) = c|\epsilon - \epsilon_0|^\nu$, where $c = 0.76$, $\epsilon_0 = 2.59$, and $\nu = -0.39$. $\nu = -0.39$ agrees well with theoretical result $\nu = -1/3$ (see main text).

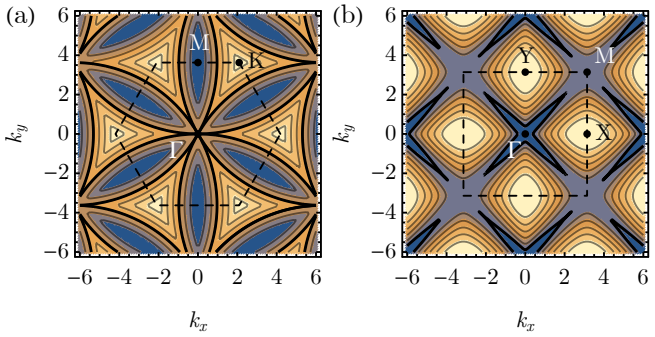


FIG. 3. (a) Fermi surface with a high-order Dirac point at the Γ point in C_6 potential Eq. (4). (b) Fermi surface with a high-order VHS of class A_2 on the high-symmetry line ΓM in D_4 potential Eq. (6). The ones passing through high-order VHS are plotted in thick black curves, among which those in (a) are perfect circles. The corresponding MBZ is plotted in dashed lines.

When $U = 0.15 v_F/L$, at energy much higher than the first set of satellite Dirac points, Γ point becomes a high-order Dirac point, where six circular Fermi surfaces intersect together as shown in Fig. 3a. The high-order Dirac point also exhibits power-law divergent DOS just like high-order VHS.

Next we consider a periodic potential with D_4 symmetry

$$U(\boldsymbol{r}) = 2U[\cos(2\pi x/L) + \cos(2\pi y/L)], \tag{6}$$

which corresponds to a square moiré superlattice. When $U = 4.71 v_F/L$, there are four high-order saddle points on four ΓM lines respectively (Fig. 3b), where the local dispersion becomes $E_{\boldsymbol{q}+\boldsymbol{V}} - E_{\boldsymbol{V}} = a q_\parallel^3 - b q_\perp^2 + \cdots$

($ab > 0$). Here $\boldsymbol{V}$ denotes the momentum of high-order saddle point, and $q_\parallel$ ($q_\perp$) is parallel (perpendicular) to the ΓM line. Such kind of saddle point can split into at most two critical points: One ordinary saddle point and one ordinary extremum, and we call it a A_2 saddle point [24], where the energy contour is beak like (Fig. 3b). Details of high-order VHS A_2 and high-order Dirac points can be found in Appendix A. The numerical DOS properties of high-order VHSs agree well with theoretical predictions in Ref.[15].

In the D_4 potential given in Eq. (6), $U(x + L/2, y + L/2) = -U(x, y)$, hence the system has an additional particle-hole symmetry $E_{\boldsymbol{k}} \to -E_{\boldsymbol{k}}$, which does not exist for C_6 potential given in Eq. (4). This is consistent with the experiment result in bulk Bi_2Te_3 crystal, where particle-hole symmetry is broken [6]. In addition, high-symmetry points in the MBZ under the D_4 potential are all time-reversal invariant, thus cannot possess nondegenerate high-order VHS.

Although a high-order saddle point requires tuning one parameter, e.g. twist angle, the power-law diverging behavior of the DOS remains present in a wide energy range even when the band structure is not exactly at high-order VHS (Fig. 5a). Taking our system of moiré surface states in C_6 potential as an example, the high-order VHS splits into three ordinary VHS and a local max/min under perturbation. Nevertheless, at temperature higher than the energy difference between the VHS and the local max/min, thermal broadened DOS is indistinguishable from the case of high-order VHS. As we will show in the following section, this energy difference is usually tiny in real materials (Fig. 5b).

In a more realistic model, we may include other ingredients in this system, such as warping effect of surface states and higher order harmonics of the scalar potential, which are beyond our model Eqs. (1) and (2). In momentum space, these effects will result in local perturbations to the energy dispersion near the high-order VHS. Consider the C_3 saddle point $E = E_{\boldsymbol{K}} + \alpha p^2 + \beta(p_x^3 - 3p_x p_y^2) + \gamma p^4 + \cdots$ at $\boldsymbol{K}$ point as an example, then the perturbations can be described by Taylor series $\Delta E = \Delta E_{\boldsymbol{K}} + \Delta\alpha p^2 + \Delta\beta(p_x^3 - 3p_x p_y^2) + \Delta\gamma p^4 + \ldots$ in momentum space. The high-order VHS of the resulting dispersion $E' \equiv E + \Delta E$ is then determined by $\alpha' \equiv \alpha + \Delta\alpha = 0$, and hence the critical value of tuning parameter UL/v_F will be perturbed from that in Fig. 2a.

Such topological argument also applies to other types of high-order VHSs [24] in general superlattices. The topology of Brillouin zone (i.e. torus) guarantees the existence of VHS in general lattices [24, 25]. In a moiré superlattice, moreover, the band structure and hence VHS can be manipulated and tuned continuously via mechanical, electrical and other means, such as tuning the twist angle or the gating voltage. Hence, we expect the Hessian matrix determinant of VHS can be tuned to zero with appropriate parameters. As a result, during the continuous tuning of moiré superlattices, we expect ordinary VHS could generally evolve into high-order VHS.

III. SUPERCONDUCTIVITY NEAR HIGH-ORDER VHS

In this section, we consider the physical consequences of high-order VHS. When the chemical potential is put at the energy of high-order VHS, interaction induced instabilities will be greatly enhanced due to the power-law divergent DOS [16–19]. In moiré surface states of topological insulators, possible interaction channels at high-order VHS are limited due to spin-momentum locking of surface states (i.e., there only exists a single spin-polarized state at every k point on the Fermi surface). In this paper, we focus on attractive interactions in the week coupling regime that is experimentally relevant.

To be specific, at the high order VHS in C_6 potential, the divergent density of states occurs near two points K and K' on the Fermi surface, where electron spins are polarized in opposite directions. We denote operators of such states as $c_{K\uparrow}$ and $c_{K'\downarrow}$ respectively, and then the only relevant (in the sense of renormalization group) electron-electron interaction reads $H_{\text{int}} = g c^\dagger_{K\uparrow} c_{K\uparrow} c^\dagger_{K'\downarrow} c_{K'\downarrow}$. Therefore, in this low energy theory, the possible instability due to the attractive interaction $g < 0$ is superconductivity. Note that the charge density wave instability that usually coexists with superconductivity is absent due to the opposite spins at K and K', while the spin density wave instability $\langle c^\dagger_{K\uparrow} c_{K'\downarrow}\rangle$ is unfavorable under attractive interaction. The absence of moire band gaps and the large Fermi velocity away from VHS also facilitate the reduction of Coulomb repulsion through retardation effects, and thus favor electron-phonon superconductivity.

To find an analytic formula for the superconducting critical temperature T_c, we employ the Anderson-Morel approximation to solve the gap equation. We assume the dimensionless interaction takes a simple form with piece wise constant attractive phonon interaction $\lambda > 0$ and repulsive interaction $\mu > 0$:

$$g(\xi, \xi') = -\lambda\Theta(\xi, \xi') + \mu, \tag{7}$$

$$\Theta(\xi, \xi') = \begin{cases} 1, & |\xi|, |\xi'| < \epsilon_D \\ 0, & \text{otherwise} \end{cases}, \tag{8}$$

where $\xi = E - E_F$ is the electron energy measured from the chemical potential E_F. Notice that $g < 0$ means attraction and $g > 0$ repulsion. When we set the chemical potential E_F to be exactly at the high-order VHS, the normalized DOS can be described by the piece wise function

$$n(\xi) = \begin{cases} |\Lambda|^{-\nu} |\xi|^\nu, & |\xi| < \Lambda \\ 1, & \Lambda < |\xi| < W \end{cases}, \tag{9}$$

where $-1 < \nu < 0$ is the power-law exponent of the DOS. Four energy scales are involved in this problem: the superconducting critical temperature T_c, the high-order VHS peak cutoff Λ, the Debye frequency ϵ_D, and the bandwidth W, which satisfy $T_c \ll \Lambda < \epsilon_D < W$.

Before we get into formal calculations, we first consider various limits with attractive interaction λ and simple expression of DOS. The critical temperature T_c is determined by the condition $\lambda\chi = 1$ with the pair susceptibility $\chi = \int_T^{\epsilon_D} n(\xi)\xi^{-1}d\xi$. When DOS is constant $n(\xi) = 1$, pair susceptibility is logarithmically divergent in temperature $\chi \sim \log(\epsilon_D/T)$, which leads to the BCS formula $T_c \sim \epsilon_D \exp(-1/\lambda)$. When DOS has an ordinary VHS with cutoff Λ, $n(\xi) = \log(\Lambda/|\xi|)$, we have $\chi \sim \log^2(\Lambda/T)$ and hence Labbé-Bok formula $T_c \sim \Lambda \exp\left(-1/\sqrt{\lambda}\right)$ [20, 21]. When DOS has a high-order VHS with cutoff Λ and power-law exponent ν, $\chi \sim (T/\Lambda)^\nu$ and hence we have the power-law formula $T_c \sim \Lambda(1/\lambda)^{1/\nu}$, where $-1 < \nu < 0$.

With interaction Eq. (7) and DOS Eq. (9), we find an exact analytic formula of the critical temperature T_c which generalizes the well known BCS formula,

$$T_c = \frac{\Lambda}{I(\nu)^{1/\nu}}\left[\frac{1}{\lambda-\mu^*} - \log\left(\frac{\epsilon_D}{\Lambda}\right) + \frac{1}{|\nu|}\right]^{-1/|\nu|}, \quad (10)$$

where $\mu^* = \mu/[1+\mu\ln(W/\epsilon_D)]$ is the screened repulsion, $I(\nu) = 2(2^{1-\nu}-1)\Gamma(\nu)\zeta(\nu)$, $\Gamma(\nu)$ and $\zeta(\nu)$ are the gamma function and the zeta function respectively, and we put $\nu = -|\nu|$ to remind the reader $-1 < \nu < 0$. We direct readers to Appendix B for detailed derivation.

In the limit $\nu \to 0^-$, the power-law dependence of the effective interaction strength $\lambda^* = \lambda - \mu^*$ disappears because the $1/\nu$ term in the bracket dominates, then Eq. (10) reduces to the BCS formula of exponential dependence, $\lim_{\nu\to 0} T_c = 1.13\epsilon_D \exp(-1/\lambda^*)$ (see Appendix B). Reproducing the correct numerical prefactor indicates that our new formula is exact.

The new formula Eq. (10) is surprisingly an analytic function of the retarded attractive interaction strength $\lambda^* = \lambda - \mu^*$ with power-law dependence. The analytic nature of the formula suggests a dramatic enhancement of superconductivity compared to ordinary metals and at ordinary VHS when λ^* is small. We compare our new formula with previous studies on various DOS in Appendix C.

We plot the transition temperature T_c as a function of effective interaction λ^* in Fig. 4a with parameters relevant to topological insulators. We find that the transition temperature T_c is enhanced enormously by the high-order VHS compared to the original Anderson-Morel result due to the power-law nature of the expression. This enhancement is robust as long as Λ and ϵ_D are at the same order.

Numerical evidence also shows that the high-order VHS has a robust enhancement effect on superconductivity even when the chemical potential is not exactly at the VHS energy $E_F \neq 0$ (Fig. 4b). We find that T_c starts to drop when E_F is comparable to T_c and stays more than half of the original T_c even when E_F is five times of T_c. This plot can be compared to future experimental data of T_c when varying the filling E_F.

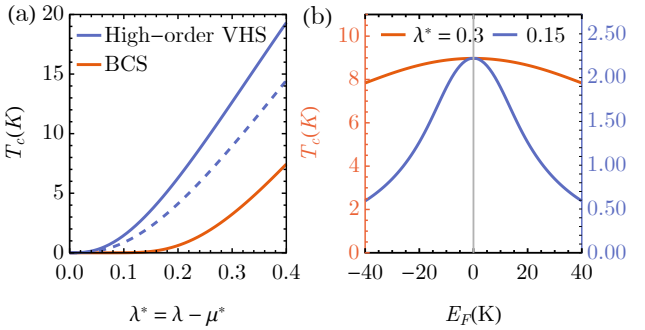


FIG. 4. (a) Transition temperature T_c at different effective interaction λ^* with $\epsilon_D = 80\,\mathrm{K}$ and $\nu = -1/3$ (the chemical potential is at the high-order VHS). The Anderson-Morel plot refers to the original Anderson-Morel formula $T_c = 1.13\epsilon_D \exp(-1/\lambda^*)$ [22], and the high-order VHS plot refers to Eq. (10). The solid blue line corresponds to $\Lambda = \epsilon_D$ and the dashed one corresponds to $\Lambda = \epsilon_D/2$, in either case T_c with a high-order VHS is much higher than the one without, especially when the effective interaction λ^* is small. (b) Transition temperature T_c when the chemical potential E_F is not exactly at the high-order VHS energy with $\Lambda = \epsilon_D/2$. The red axis on the left and the blue axis on the right correspond to the red and blue curve respectively, both of which are T_c in Kelvin. T_c starts to drop when E_F is comparable to T_c.

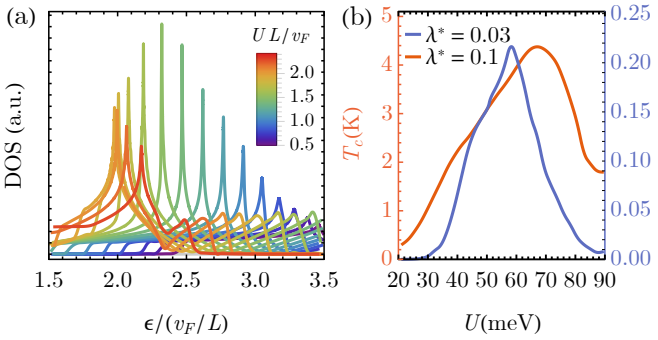


FIG. 5. (a) DOS of moiré surface states under the C_6 potential in Eq. (4) with various U, which has a sharp high-order-VHS-like peak in a wide range of U. (b) Transition temperature T_c at different U (the chemical potential is held exactly at the VHS) with $\epsilon_D = 80\,\mathrm{K}$ and $v_F/L = 435\,\mathrm{K}$. The red axis on the left and the blue axis on the right correspond to the red and blue curve respectively, both of which are T_c in Kelvin. T_c shows a wide peak around the potential that corresponds to high-order VHS.

Now we come back to the moiré surface states in C_6 potential to discuss the effect of perturbing the band structure away from high-order VHS. In fact, the DOS has a sharp high-order-VHS-like peak in a wide range of U (Fig. 5a), which suggests a significant enhancement of

superconductivity even when the band structure is not exactly at high-order VHS. We solve the gap equation numerically with the chemical potential held exactly at the VHS. As shown in Fig. 5b, T_c is enhanced in a wide range of U, and the window of U within which T_c is enhanced can be especially wide when λ^* is large. This also means the energy difference between the VHS and the local max/min is at the order of sub-Kelvin even when the potential is perturbed tens of meVs away from the high-order VHS.

Finally we discuss several possible systems to realize our model of Dirac fermion in a periodic potential and the phonon-induced superconductivity within. A prototypical system is the moiré topological insulator surface states, where the effective potential can be comparable to the kinetic energy at scale v_F/L. In real TIs, the Dirac velocity v_F can be a few eV Å's [26–28], and the moiré supercell constant L can be several or even tens of nm's depending on the lattice mismatch [5–9], then the energy scale v_F/L is at order of tens of meVs, which is comparable to the effective potential at moiré scale [29–31]. Furthermore, Bi_2Se_3 is believed to have strong electron-phonon interaction [32, 33]. Great effort has been put into extract the electron-phonon coupling strength λ of Bi_2Se_3 both theoretically and experimentally, and most studies fall into the range from $\lambda = 0.2$ to 0.5 (Fig. 4) [34–37]. Bi_2Se_3 also has a relatively large dielectric constant $\epsilon > 50$ [32, 33], and the bandwidth of topological surface bands reaches at least 800 meV [38], so the renormalized Coulomb repulsion μ^* is negligible, i.e. $\lambda^* \approx \lambda$. With the numbers given, we anticipate that superconductivity can occur on moire surface states of topological insulators with transition temperature up to $T_c \sim 10\,\mathrm{K}$.

IV. CONCLUSION

In this work, we study the moiré topological insulator surface states using a continuum model of Dirac electrons moving in periodic potentials at moiré scale. Within the continuum model, we identify various types of high-order VHS. We further compute the superconducting transition temperature T_c when the chemical potential is close to the high-order VHS. When exactly at the high-order VHS, we give an analytic formula of T_c, showing a power-law instead of exponential dependence of the retarded electron-phonon interaction strength. This result suggests a significantly enhanced superconductivity at high-order VHS, especially when the electron-phonon interaction is weak. In the end, we discuss several real materials that can demonstrate the enhancement of superconductivity due to high-order VHS.

Note added.– After this work is completed, we became aware of a related and independent work [39].

ACKNOWLEDGMENTS

We acknowledge Hiroki Isobe, Yang Zhang and Yi-Zhuang You for helpful discussion. This work is supported by DOE Office of Basic Energy Sciences, Division of Materials Sciences and Engineering under Award DE-SC0018945. LF is partly supported by the Simons Investigator award from the Simons Foundation.

Appendix A: High-order Dirac point and high-order VHS of type A_2

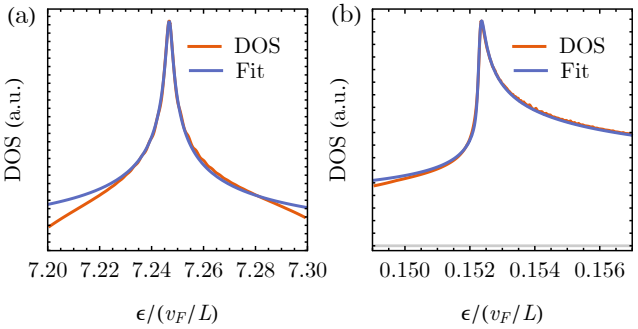


FIG. 6. (a) DOS of the relevant bands around the high-order Dirac point. The fitting is given by $N(\epsilon) = c|\epsilon - \epsilon_0|^\nu + n$, where $c = 0.047$, $\epsilon_0 = 7.25$, $\nu = -0.33$, and $n = 0.89$. (b) DOS of the relevant band around the high-order VHS of class A_2. The fitting is given by $N(\epsilon) = C_\pm|\epsilon - \epsilon_0|^\nu$ (see Eq. (3) for definition) with $C_- = 0.35$, $C_+ = 1.82C_-$, $\epsilon_0 = 0.152$, and $\nu = -0.20$. Both ν and C_+/C_- agrees well with the theoretical prediction.

In this appendix, we describe the high-order Dirac point and high-order VHS of class A_2 introduced in the main text in more details. Under C_6 potential, the high-order Dirac point is identified at the Γ point at energy much higher than the first set of satellite Dirac points. Three secondary Dirac cones in this system are lifted by the C_6 potential, and the middle one is in general flattened (Fig. 7a). When $U = 0.15v_F/L$, the Γ point becomes a high-order Dirac point, which also exhibits power-law divergent DOS with $\nu = -1/3$ (Fig. 6a).

Under D_4 potential, the high-order VHS of class A_2 is identified on the high-symmetry line ΓM in the primary Dirac cone at $U = 4.71v_F/L$ (Fig. 7b). In this case, the divergence is in perfect agree with the theoretical prediction $\nu = -1/6$ and the asymmetry ratio between the high energy and low energy side is close to $\sqrt{3}$ as predicted in Ref. [15]. (Fig. 6b).

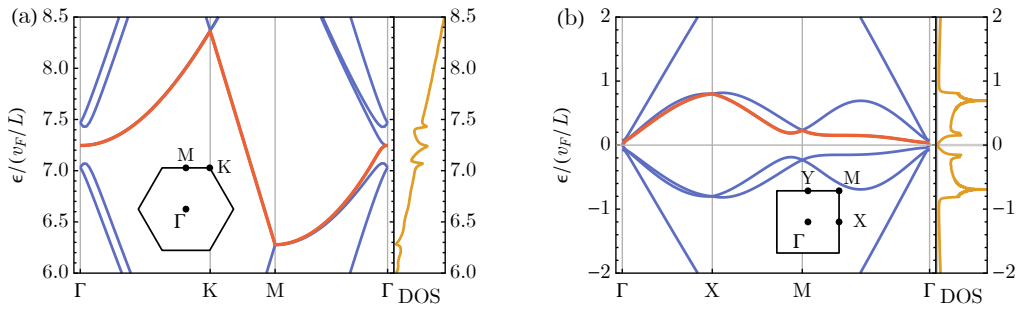


FIG. 7. (a) Spectrum and DOS of Dirac fermion in a C_6 potential with $U = 0.15 v_F/L$. The high-order Dirac point has been identified at the Γ point at energy much higher than the first set of satellite Dirac points (highlighted in red). (b) Spectrum and DOS of Dirac fermion in a D_4 potential with $U = 4.71 v_F/L$. The high-order VHS of class A_2 has been identified on the high-symmetry line ΓM in the primary Dirac cone (highlighted in red).

Appendix B: Solution to the BCS gap equation at high-order VHS

In this appendix, we solve the BCS gap equation at high-order VHS within Anderson-Morel approximation [40, 41],

$$\Delta_k = -\sum_{k'} V_{k,k'} \frac{\Delta_{k'}}{2E_{k'}} \tanh \frac{E_{k'}}{2T} \tag{B1}$$

where Δ_k is the superconducting gap, and $E_k = \sqrt{\xi_k^2 + \Delta_k^2}$ is the quasiparticle energy. Due to the complexity of the gap equation, now we proceed within the Anderson-Morel approximation [22], in which both the interaction strength and the gap are assumed to be piece wise constant. We consider four energy scales: the superconducting gap $\Delta \sim T_c$, the high-order VHS peak cutoff Λ, the Debye frequency ϵ_D, and the bandwidth W, with $T_c \ll \Lambda < \epsilon_D < W$. Now we assume that the dimensionless interaction takes a simple form: piece wise constant attractive phonon interaction λ and a repulsive Coloumb interaction μ,

$$g(\xi, \xi') = -\lambda \Theta(\xi, \xi') + \mu, \tag{B2}$$

$$\Theta(\xi, \xi') = \begin{cases} 1, & |\xi|, |\xi'| < \epsilon_D \\ 0, & \text{otherwise} \end{cases}, \tag{B3}$$

which is normalized with the constant DOS N_0 away from the van Hove singularity, $V_{\xi,\xi'} = g(\xi, \xi')/N_0$. The normalized density of state $n(\xi) = N(\xi)/N_0$, however, is modified from the original Anderson-Morel model to account for the high-order VHS. For now we set the chemical potential E_F to be exactly at the high-order van Hove singularity,

$$n(\xi) = \begin{cases} C\,|\xi|^\nu, & |\xi| < \Lambda \\ 1, & \Lambda < |\xi| < W \end{cases} \tag{B4}$$

where $-1 < \nu < 0$ is the power-law exponent of the DOS. The continuity condition enforced that $C = |\Lambda|^{-\nu}$. Within the Anderson-Morel approximation, the gap also takes a simple form,

$$\Delta(\xi) = \begin{cases} \Delta_1, & |\xi| < \omega_D \\ \Delta_2, & \omega_D < |\xi| < W \end{cases} \tag{B5}$$

Plugging in $N(\xi')$ and $V(\xi, \xi')$, the gap equation becomes

$$\begin{pmatrix} \Delta_1 \\ \Delta_2 \end{pmatrix} = \begin{pmatrix} (\lambda - \mu)\left\{ I(\nu)\left(\frac{T}{\Lambda}\right)^\nu + \log\left(\frac{\epsilon_D}{\Lambda}\right) + \frac{1}{\nu} \right\} & -\mu \log\left(W/\epsilon_D\right) \\ -\mu\left\{ I(\nu)\left(\frac{T}{\Lambda}\right)^\nu + \log\left(\frac{\epsilon_D}{\Lambda}\right) + \frac{1}{\nu} \right\} & -\mu \log\left(W/\epsilon_D\right) \end{pmatrix} \begin{pmatrix} \Delta_1 \\ \Delta_2 \end{pmatrix} \tag{B6}$$

where $I(\nu) = 2(2^{1-\nu} - 1)\Gamma(\nu)\zeta(\nu)$, $\Gamma(\nu)$ and $\zeta(\nu)$ are the gamma function and the zeta function respectively. Here we use an important integral,

$$\int_0^{\epsilon_D} \mathrm{d}\xi n(\xi) \frac{\tanh\left(\beta\xi/2\right)}{\xi} = \left(\frac{T}{\Lambda}\right)^\nu \left(I(\nu) - \int_{\beta\Lambda}^{\infty} \mathrm{d}x x^{\nu-1} \right) + \int_{\beta\Lambda}^{\beta\epsilon_D} \frac{\mathrm{d}x}{x}, \qquad I(\nu) \equiv \int_0^\infty \mathrm{d}x x^{\nu-1} \tanh\left(\frac{x}{2}\right), \tag{B7}$$

where we used $T_c \ll \Lambda$. Solving the consistency equation gives the critical temperature

$$T_c = \frac{\Lambda}{I(\nu)^{1/\nu}} \left[\frac{1}{\lambda - \mu^*} - \log\left(\frac{\epsilon_D}{\Lambda}\right) + \frac{1}{|\nu|} \right]^{-1/|\nu|}. \tag{B8}$$

Appendix C: Comparison of the T_c formula with previous works

In this appendix, we compare our result with previous works with various DOS (Fig. 8a). In Anderson and

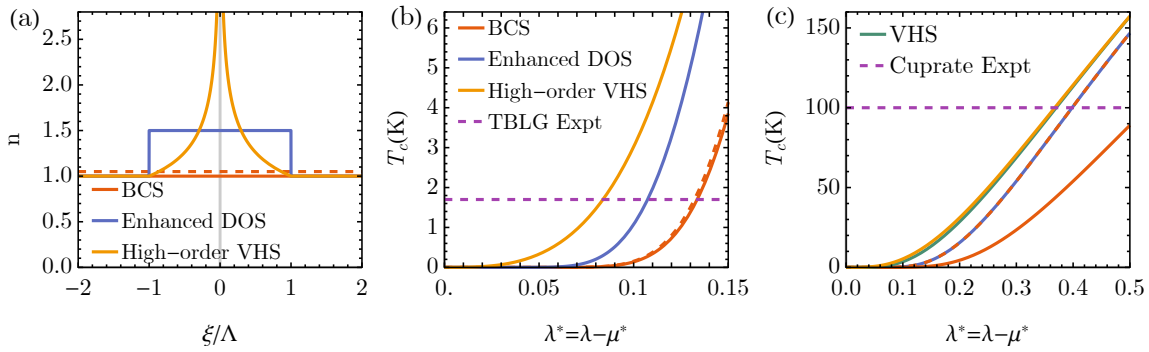


FIG. 8. (a) Schematic plot of the DOS in different scenarios ($\nu = -1/3$ for the high-order VHS scenario). The rescaled DOS in the BCS scenario is plotted with a red dashed line with $\epsilon_D = 10\Lambda$ (see text for definiton). (b-c) Transition temperature T_c at different retarded interaction $\lambda^* = \lambda - \mu^*$ with parameters relevant to (b) twisted bilayer graphene (tBLG) and (c) cuprate superconductor. The red dashed line represents using rescaled DOS in the BCS scenario. Detailed description for each line is in the text. In (b), we pick $\epsilon_D = 230\,\text{meV}$, $\Lambda = 5\,\text{meV}$, $\nu = -1/3$. In (c), we pick $\epsilon_D = 50\,\text{meV}$, $\Lambda = 50\,\text{meV}$, $\nu = -1/4$.

Morel's original work, the transition temperature T_c is derived at constant density of states $n(\xi) = 1$ (Fig. 8a), $T_c = 1.13\epsilon_D \exp\left(-\frac{1}{\lambda-\mu^*}\right)$ [22]. To show how our result reduces to this Anderson-Morel formula in the limit $|\nu| \to 0$, we first use the asymptotic form of the gamma function and the zeta function at $|\nu| \to 0$ to find $I(\nu) \sim -\frac{1}{\nu} + \gamma + \log(2/\pi)$, where γ is Euler's constant. Then we plug in to find T_c,

$$T_c \sim \Lambda \left(\frac{n + \gamma + \log(2/\pi)}{n + \frac{1}{\lambda-\mu^*} - \log\left(\frac{\epsilon_D}{\Lambda}\right)} \right)^n \tag{C1}$$

$$\sim \Lambda \left\{ 1 + \log\left[\frac{2}{\pi} e^\gamma \frac{\epsilon_D}{\Lambda} \exp\left(-\frac{1}{\lambda - \mu^*} \right) \right] \frac{1}{n} \right\}^n \tag{C2}$$

where $n = 1/|\nu|$. Finally, the definition of Euler's number e simplifies the formula,

$$\lim_{\nu \to 0^-} T_c = \frac{2}{\pi} e^\gamma \epsilon_D \exp\left(-\frac{1}{\lambda - \mu^*} \right) \tag{C3}$$

where $2e^\gamma/\pi = 1.13$ recovers the correct numerical prefactor in the BCS formula, indicating that our new formula is exact.

Tang *et al.* generalized Anderson and Morel's result to the enhanced DOS scenario in the context of topological crystalline insulator interface superconductivity, where $n(\xi) = \alpha$ within the flat band width Λ (Fig. 8a) [4, 42],

$$T_c = 1.13\Lambda \left(\frac{\epsilon_D}{\Lambda} \right)^{1/\alpha} \exp\left(-\frac{1}{\alpha(\lambda - \mu^*)} \right) \tag{C4}$$

The VHS plot refers to Labbé and Bok's work in the context of cuprate superconductors in the limit $\Lambda \gg \epsilon_D$, where $n(\xi) = n_1 \log(\Lambda/\xi) + n_0$ within the VHS peak cutoff Λ [20, 21],

$$T_c = \frac{\Lambda}{2} \exp\left(0.819 + \frac{1}{n_1} - \sqrt{F} \right), \tag{C5}$$

where $F \equiv \left(\frac{1}{n_1} + 0.819\right)^2 + \left(\log\left(\frac{\epsilon_D}{\Lambda}\right)\right)^2 - 2 - \frac{2}{n_1}\left(\log\left(\frac{2.28\epsilon_D}{\Lambda}\right) - \frac{1}{\lambda-\mu^*}\right)$. Here μ^* is renormalized slightly differently from the usual Anderson-Morel screening. We refer the reader to Ref.[21] for a more detailed discussion.

Heikkilä *et al.* also considered a scenario with power-law divergent DOS $N(\xi) = \xi^\nu/\Lambda^\nu$ in the context of the multiple Dirac point [43–45]. Unlike us, they work in the limit $\Lambda \gg \epsilon_D$. In our language, their formula can be rewritten as

$$T_c = \frac{(2(\nu+1))^{1/\nu}}{2J(\nu)^{1/\nu}} \Lambda \left(\frac{\epsilon_D}{\Lambda} \right)^{1/|\nu|-1} \left(\frac{1}{\lambda} \right)^{-1/|\nu|}, \tag{C6}$$

where $J(\nu) = \Gamma(-\nu/2)\Gamma((3+\nu)/2)/\sqrt{\pi}$.

Now we compare the transition temperature T_c among these various DOS setups. It is important to normalize the number of states to make a fair comparison. If we normalize the number of states within the bandwidth W, the difference among various DOS setup are negligible since $W \gg \Lambda$. If we instead normalize the number of states within the bandwidth Λ, we find $\alpha = 1/(\nu+1)$ in the enhanced DOS scenario and $n_1 = -1 + 1/(\nu+1)$ in the VHS scenario. We also include a rescaled DOS for the BCS scenario by normalizing the number of states within Debye frequency ϵ_D (Fig. 8a). We plot T_c as a function of the retarded interaction $\lambda^* = \lambda - \mu^*$ in Fig. 8b-c, with parameters relevant for tBLG in Fig. 8b, and those for cuprates in Fig. 8c. In particular, we pick $\nu = -1/3$ for tBLG and $\nu = -1/4$ for cuprates, which corresponds to the leading order high-order VHS for systems with C_3 symmetry and D_4 symmetry respectively. The tBLG plot is not compatible with the VHS result since Labbé and Bok assumes that the flat band range Λ is much larger compared to the Debye frequency ϵ_D, which does not hold in tBLG.

[1] Eva Y. Andrei and Allan H. MacDonald, "Graphene bilayers with a twist," (2020), arXiv:2008.08129.

[2] Leon Balents, Cory R. Dean, Dmitri K. Efetov, and Andrea F. Young, "Superconductivity and strong correlations in moiréflat bands," Nature Physics **16**, 725–733 (2020).

[3] Stephen Carr, Shiang Fang, and Efthimios Kaxiras, "Electronic-structure methods for twisted moirélayers," Nature Reviews Materials **5**, 748–763 (2020).

[4] Evelyn Tang and Liang Fu, "Strain-induced partially flat band, helical snake states and interface superconductivity in topological crystalline insulators," Nature Physics **10**, 964–969 (2014).

[5] Y. Liu, Y. Y. Li, S. Rajput, D. Gilks, L. Lari, P. L. Galindo, M. Weinert, V. K. Lazarov, and L. Li, "Tuning dirac states by strain in the topological insulator Bi_2Se_3," Nature Physics **10**, 294–299 (2014).

[6] Koen Schouteden, Zhe Li, Taishi Chen, Fengqi Song, Bart Partoens, Chris Van Haesendonck, and Kyungwha Park, "Moirésuperlattices at the topological insulator bi2te3," Scientific Reports **6**, 20278 (2016).

[7] Anthony Vargas, Fangze Liu, Christopher Lane, Daniel Rubin, Ismail Bilgin, Zachariah Hennighausen, Matthew DeCapua, Arun Bansil, and Swastik Kar, "Tunable and laser-reconfigurable 2d heterocrystals obtained by epitaxial stacking of crystallographically incommensurate Bi_2Se_3 and MoS_2 atomic layers," Science Advances **3** (2017), 10.1126/sciadv.1601741.

[8] Zachariah Hennighausen, Christopher Lane, Abdelkrim Benabbas, Kevin Mendez, Monika Eggenberger, Paul M. Champion, Jeremy T. Robinson, Arun Bansil, and Swastik Kar, "Oxygen-induced in situ manipulation of the interlayer coupling and exciton recombination in Bi_2Se_3/MoS_2 2d heterostructures," *ACS Applied Materials & Interfaces*, ACS Applied Materials & Interfaces **11**, 15913–15921 (2019).

[9] Zachariah Hennighausen, Christopher Lane, Ioana Gianina Buda, Vineet K. Mathur, Arun Bansil, and Swastik Kar, "Evidence of a purely electronic two-dimensional lattice at the interface of TMD/Bi_2Se_3 heterostructures," Nanoscale **11**, 15929–15938 (2019).

[10] Can-Li Song, Yi-Lin Wang, Ye-Ping Jiang, Yi Zhang, Cui-Zu Chang, Lili Wang, Ke He, Xi Chen, Jin-Feng Jia, Yayu Wang, Zhong Fang, Xi Dai, Xin-Cheng Xie, Xiao-Liang Qi, Shou-Cheng Zhang, Qi-Kun Xue, and Xucun Ma, "Topological insulator Bi_2Se_3 thin films grown on double-layer graphene by molecular beam epitaxy," Applied Physics Letters **97**, 143118 (2010).

[11] Yilin Wang, Yeping Jiang, Mu Chen, Zhi Li, Canli Song, Lili Wang, Ke He, Xi Chen, Xucun Ma, and Qi-Kun Xue, "Scanning tunneling microscopy of interface properties of Bi_2Se_3 on FeSe," Journal of Physics: Condensed Matter **24**, 475604 (2012).

[12] Jeong Heum Jeon, Won Jun Jang, Jong Keon Yoon, and Se-Jong Kahng, "Metal-supported high crystalline Bi_2Se_3 quintuple layers," Nanotechnology **22**, 465602 (2011).

[13] Shuigang Xu, Yu Han, Xiaolong Chen, Zefei Wu, Lin Wang, Tianyi Han, Weiguang Ye, Huanhuan Lu, Gen Long, Yingying Wu, Jiangxiazi Lin, Yuan Cai, K. M. Ho, Yuheng He, and Ning Wang, "van der Waals epitaxial growth of atomically thin Bi_2Se_3 and thickness-dependent topological phase transition," *Nano Letters*, Nano Letters **15**, 2645–2651 (2015).

[14] Jin-Peng Xu, Mei-Xiao Wang, Zhi Long Liu, Jian-Feng Ge, Xiaojun Yang, Canhua Liu, Zhu An Xu, Dandan Guan, Chun Lei Gao, Dong Qian, Ying Liu, Qiang-Hua Wang, Fu-Chun Zhang, Qi-Kun Xue, and Jin-Feng Jia, "Experimental detection of a majorana mode in the core of a magnetic vortex inside a topological insulator-superconductor $Bi_2Te_3/NbSe_2$ heterostructure," Phys. Rev. Lett. **114**, 017001 (2015).

[15] Noah F. Q. Yuan, Hiroki Isobe, and Liang Fu, "Magic of high-order van hove singularity," Nature Communications **10**, 5769 (2019).

[16] Rahul Nandkishore, L. S. Levitov, and A. V. Chubukov, "Chiral superconductivity from repulsive interactions in doped graphene," Nature Physics **8**, 158–163 (2012).

[17] Rahul Nandkishore and Andrey V. Chubukov, "Interplay of superconductivity and spin-density-wave order in doped graphene," Phys. Rev. B **86**, 115426 (2012).

[18] Hiroki Isobe and Liang Fu, "Supermetal," arXiv e-prints , arXiv:1905.05188 (2019), arXiv:1905.05188 [cond-mat.str-el].

[19] Francisco Guinea and Niels R. Walet, "Electrostatic effects, band distortions, and superconductivity in twisted graphene bilayers," Proceedings of the National Academy of Sciences **115**, 13174–13179 (2018), https://www.pnas.org/content/115/52/13174.full.pdf.

[20] J Labbé and J Bok, "Superconductivity in alcaline-earth-substituted La_2CuO_4: A theoretical model," Europhysics Letters (EPL) **3**, 1225–1230 (1987).

[21] J. Bok, "Superconductivity in the cuprates. the van hove scenario," Physica C: Superconductivity **209**, 107 – 112 (1993).

[22] P. Morel and P. W. Anderson, "Calculation of the superconducting state parameters with retarded electron-phonon interaction," Phys. Rev. **125**, 1263–1271 (1962).

[23] Cheol-Hwan Park, Li Yang, Young-Woo Son, Marvin L. Cohen, and Steven G. Louie, "Anisotropic behaviours of massless dirac fermions in graphene under periodic potentials," Nature Physics **4**, 213–217 (2008).

[24] Noah F. Q. Yuan and Liang Fu, "Classification of critical points in energy bands based on topology, scaling, and symmetry," Phys. Rev. B **101**, 125120 (2020).

[25] Léon Van Hove, "The occurrence of singularities in the elastic frequency distribution of a crystal," Phys. Rev. **89**, 1189–1193 (1953).

[26] Y. L. Chen, J. G. Analytis, J.-H. Chu, Z. K. Liu, S.-K. Mo, X. L. Qi, H. J. Zhang, D. H. Lu, X. Dai, Z. Fang, S. C. Zhang, I. R. Fisher, Z. Hussain, and Z.-X. Shen, "Experimental realization of a three-dimensional topological insulator, Bi_2Te_3," Science **325**, 178–181 (2009).

[27] Y. Xia, D. Qian, D. Hsieh, L. Wray, A. Pal, H. Lin, A. Bansil, D. Grauer, Y. S. Hor, R. J. Cava, and M. Z. Hasan, "Observation of a large-gap topological-insulator class with a single dirac cone on the surface," Nature Physics **5**, 398–402 (2009).

[28] D. Hsieh, D. Qian, L. Wray, Y. Xia, Y. S. Hor, R. J. Cava, and M. Z. Hasan, "A topological dirac insulator in a quantum spin hall phase," Nature **452**, 970–974 (2008).

[29] Alexander Kerelsky, Leo J. McGilly, Dante M. Kennes, Lede Xian, Matthew Yankowitz, Shaowen Chen, K. Watanabe, T. Taniguchi, James Hone, Cory Dean, Angel Rubio, and Abhay N. Pasupathy, "Maximized electron interactions at the magic angle in twisted bilayer graphene," Nature **572**, 95–100 (2019).

[30] Fengcheng Wu, Timothy Lovorn, Emanuel Tutuc, Ivar Martin, and A. H. MacDonald, "Topological insulators in twisted transition metal dichalcogenide homobilayers," Phys. Rev. Lett. **122**, 086402 (2019).

[31] Yang Zhang, Noah F. Q. Yuan, and Liang Fu, "Moiré quantum chemistry: charge transfer in transition metal dichalcogenide superlattices," (2019), arXiv:1910.14061 [cond-mat.str-el].

[32] Y. Xia, D. Qian, D. Hsieh, L. Wray, A. Pal, H. Lin, A. Bansil, D. Grauer, Y. S. Hor, R. J. Cava, and M. Z. Hasan, "Observation of a large-gap topological-insulator class with a single dirac cone on the surface," Nature Physics **5**, 398–402 (2009).

[33] D. Hsieh, Y. Xia, D. Qian, L. Wray, J. H. Dil, F. Meier, J. Osterwalder, L. Patthey, J. G. Checkelsky, N. P. Ong, A. V. Fedorov, H. Lin, A. Bansil, D. Grauer, Y. S. Hor, R. J. Cava, and M. Z. Hasan, "A tunable topological insulator in the spin helical dirac transport regime," Nature **460**, 1101 EP – (2009).

[34] S. Das Sarma and Qiuzi Li, "Many-body effects and possible superconductivity in the two-dimensional metallic surface states of three-dimensional topological insulators," Phys. Rev. B **88**, 081404 (2013).

[35] Xuetao Zhu, L. Santos, C. Howard, R. Sankar, F. C. Chou, C. Chamon, and M. El-Batanouny, "Electron-phonon coupling on the surface of the topological insulator Bi_2Se_3 determined from surface-phonon dispersion measurements," Phys. Rev. Lett. **108**, 185501 (2012).

[36] Richard C. Hatch, Marco Bianchi, Dandan Guan, Shining Bao, Jianli Mi, Bo Brummerstedt Iversen, Louis Nilsson, Liv Hornekær, and Philip Hofmann, "Stability of the Bi_2Se_3(111) topological state: Electron-phonon and electron-defect scattering," Phys. Rev. B **83**, 241303 (2011).

[37] Z.-H. Pan, A. V. Fedorov, D. Gardner, Y. S. Lee, S. Chu, and T. Valla, "Measurement of an exceptionally weak electron-phonon coupling on the surface of the topological insulator Bi_2Se_3 using angle-resolved photoemission spectroscopy," Phys. Rev. Lett. **108**, 187001 (2012).

[38] Wenwen Zhou, *STM probe on the surface electronic states of spin-orbit coupled materials*, Ph.D. thesis, Boston College (2014).

[39] Jennifer Cano, Shiang Fang, J. H. Pixley, and Justin H. Wilson, "A moiré superlattice on the surface of a topological insulator," (2020), arXiv:2010.09726.

[40] J. Bardeen, L. N. Cooper, and J. R. Schrieffer, "Microscopic theory of superconductivity," Phys. Rev. **106**, 162–164 (1957).

[41] J. Bardeen, L. N. Cooper, and J. R. Schrieffer, "Theory of superconductivity," Phys. Rev. **108**, 1175–1204 (1957).

[42] Evelyn Tang, *Topological phases in narrow-band systems*, Ph.D. thesis, Massachusetts Institute of Technology (2015).

[43] T. T. Heikkilä, N. B. Kopnin, and G. E. Volovik, "Flat bands in topological media," JETP Letters **94**, 233 (2011).

[44] Risto Ojajärvi, Timo Hyart, Mihail A. Silaev, and Tero T. Heikkilä, "Competition of electron-phonon mediated superconductivity and stoner magnetism on a flat band," Phys. Rev. B **98**, 054515 (2018).

[45] Teemu J. Peltonen, Risto Ojajärvi, and Tero T. Heikkilä, "Mean-field theory for superconductivity in twisted bilayer graphene," Phys. Rev. B **98**, 220504 (2018).